Improvement of Underwater Laser Ranging Accuracy Based on Wavelet Time-Frequency Analysis

Xin Yu Liu, Su Hui Yang, Junwen Ji, Zhen Xu, and Yingqi Liao

***Abstract*—A laser time-frequency analysis ranging method based on wavelet transform for underwater target detection has been proposed in this paper. The band-pass filtering characteristics of the wavelet transform are combined with the energy conservation of the signal time-frequency domain during the wavelet time-frequency decomposition process of the echo signal. Binary spline interpolation is used to obtain the time-frequency correspondence matrix of the echo signal energy. In this method, the frequency range of the target echo signal is selected through the multi-layer wavelet time-domain decomposition process. The time-frequency energy matrix of the echo signal is extracted in the frequency range, and these frequencies are integrated to determine the restored time-domain echo signal. The corresponding delay of the target is determined by the peak detection method, and the target distance information is retrieved. The emission source is a 532 nm pulsed laser with a repetition frequency of 50 kHz, a pulse width of 1 ns, and average power of 3 W. The APD detector and the acquisition system with a bandwidth of 1 G are used to receive the echo signal. By detecting diffuse reflection targets in the water with an attenuation length of 10, the signal processing method can reduce the ranging error from 11.83 cm to less than 4 cm.**

***Index Terms*—Time-domain decomposition, time-frequency decomposition, wavelet transform.**

I. Introduction

LIDAR has become an effective method for underwater target detection [1] due to its high spatial resolution and flexible platform. However, there are unfavorable factors such as scattering in the propagation of laser in water, which lead to the broadening of the pulse, the dispersion of the beam, and the reduction of ranging accuracy and imaging resolution. Time gating [2], [3], [4], [5], [6], carrier modulation [7], vortex field spatial filtering [8], [9], [10], and blind signal separation [11], [12] are some of the commonly used anti-scattering techniques. In recent years, the time gating method was mostly combined with the photon counting detection system. The time gating method was mostly combined with the photon counting detection system, by setting the threshold [18], [19] the influence of backscattering [20], [21], [22], [23] was reduced [24], [25], [26], [27]. However, when the time gating method is applied to underwater detection, it is necessary to estimate the approximate position of the detected object to achieve accurate target detection. In carrier modulation method, the intensity of the carrier was modulated at a radio frequency (RF), when the modulation frequency is higher than the cut off frequency, the modulation from the scattering cutter is averaged but the modulation information in the target echo is more or less maintained. A proper filter is applied to filter out the low frequency scattering clutter and keep the target signal, therefore, reduce the influence of scattering. In vortex field spatial filtering, the target reflected Gaussian beam is converted into optical vortices through Spiral Phase Plate (SPP), whereas the scattering clutters could not be converted because of the loss of spatial coherence. Thus, they are spatially separated by an SPP and the scattering clatters can be blocked.The echo light passes through the spiral phase plate to form the annular optical vortex of the target signal, whereas the scattered clutter is gathered inside to realize the spatial separation of the target signal and the scattered clutter. The blind signal separation technique [28] relies on the assumption that the mixed signals are statistically independent. It constructs an echo signal observation matrix and performs corresponding statistics to separate the target signal and the scattered clutter. To achieve separation using blind signal separation technology, the number of independent observations must be greater than or equal to the number of separation sources. In this paper, an underwater laser time-frequency analysis ranging method based on wavelet transform is proposed. This can separate the target signal from the scattered clutter with only one set of echo signals and can realize underwater detection without estimating the target's spatial position.

The method is based on the energy conservation of the time-domain signal and the corresponding frequency-domain signal. The band-pass filtering characteristics of the wavelet transform are combined with the energy conservation of the signal in time-frequency domain during the wavelet time-frequency decomposition process of the echo signal. With pulsed light as the emission source, the frequency spectrum of the echo signal includes not only the frequency range corresponding to the scattering and the target signal but also the high-frequency noise interference from the detector or other electronic components. The wavelet time-frequency decomposition process is as follows: Firstly, the high-frequency clutter mainly composed of electromagnetic noise in the echo signal is filtered out through the multi-layer wavelet time-domain decomposition. Then, the time-frequency energy distribution function of the

Manuscript received 5 July 2022; revised 11 September 2022; accepted 30 September 2022. Date of publication 4 October 2022; date of current version 13 October 2022. This work was supported by the National Natural Science Foundation of China under Grant 61835001. *(Corresponding author: Su Hui Yang.)*

The authors are with the Department of School of Optics and Photonics, Beijing Institute of Technology, Beijing 100081, China (e-mail: 3120205324@bit.edu.cn; suhuiyang@bit.edu.cn; 18010095217@163.com; 3120215332@bit.edu.cn; 1837936162@qq.com).

Digital Object Identifier 10.1109/JPHOT.2022.3211711

echo signal is established by the binary spline interpolation. The time-frequency energy presents different distributions with the change in underwater transmission distance and water turbidity. In these time-frequency energy distributions, the target echo can keep the high-frequency information of the echo. In this method, a time-frequency energy matrix of the echo signal is constructed by multi-layer wavelet time-frequency decomposition. For pulsed light underwater detection, the area with higher frequency in the time-frequency energy matrix was selected as target echo andused to extract the waveform in time domain by integrating the energy distribution in the matrix with respect to frequency. The corresponding delay of the target is determined by peak detection method, and the target distance information is retrieved. In the time-frequency energy distribution matrix, the low-frequency energy region was dominated by scattering and discarded before restoring the waveform in time domain therefore the influence of scattering was filtered out in part.

II. Theoretical Principles

A. Wavelet Time Domain Decomposition

The wavelet transform is written as:

$$WT(A,t') = \int_{-\infty}^{\infty} \frac{1}{\sqrt{A}} f(t)\psi\left(\frac{t-t'}{A}\right)dt = \int_{-\infty}^{\infty} f(t)\psi_{A,t'}(t)dt \quad (1)$$

Where, $\psi_{A,t'}(t)$ denotes the wavelet basis function [29], and $f(t)$ represents the original signal. The wavelet basis function $\psi_{A,t'}(t)$ is quite similar to the original signal, whereas its function is similar to that of the window function. The window function corresponding to the wavelet basis function $\psi_{A,t'}(t)$ is adaptive [30], when a high-frequency signal is detected, the scale parameter A of the wavelet basis function $\psi_{A,t'}(t)$ becomes smaller, and the corresponding window in frequency domain increases. When a low-frequency signal dominates the detection, the scale parameter A of the wavelet basis function $\psi_{A,t'}(t)$ increases, and the corresponding window reduces.

Multi-layer wavelet time-domain decomposition [31], [32], [33] includes discretizing and decomposing the original signal $f(t)$ based on wavelet transform and the frequency range of the acquisition system. Among these, the wavelet basis function, which is the most similar to the original signal waveform, constitutes an approximate signal $WT(A,t')$, whereas the rest are detail signals $WT(a,t'')$. Fig. 1 highlights the underwater echo signal with an analog sampling rate of 2.5 GHz and a pulse width of 1 ns, corresponding to the frequency range of the echo signal [0∼1 GHz]. After the first layer of the wavelet time-domain decomposition, the signal is further divided into two parts based on the frequency range: the corresponding frequency range of the approximate signal is [0∼1.25 GHz], and the corresponding frequency range of the detail signal is [1.25 GHz∼2.5 GHz].

As demonstrated in Fig. 1, the intensity of the detailed wavelet time-domain signal at the target position is significantly higher than that at the other parts. When only one decomposition is performed, the frequency resolution of the approximate wavelet basis function is $f' = \frac{f_{mid}}{(f_m/(0.5f_{mid}))\times 2^1} = 0.3125$ GHz. In this case, the part of the target signal corresponding to the frequency range (1 GHz∼1.25 GHz] cannot be distinguished, therefore, only the detailed wavelet time-domain signal may contain a part of the target signal.

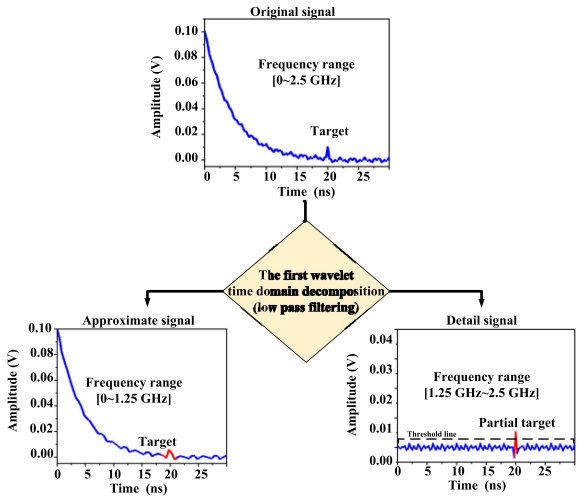

Fig. 1. The first-layer wavelet time-domain decomposition process.

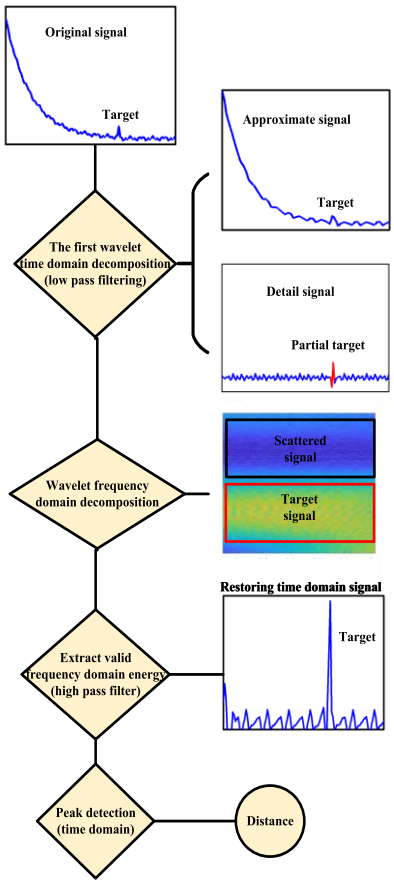

Fig. 2. The detection process of underwater target by underwater laser time-frequency analysis method based on wavelet transform.

B. Ranging Method Based on Time-Frequency Decomposition

Wavelet time-frequency analysis is based on energy conservation in signal time-frequency space. To establish a time-frequency energy matrix, binary spline interpolation is used. This method further enhances the frequency resolution of the wavelet basis function. A time-frequency energy matrix $P_{n\times m}(WT_f, Wf_T)$ with constant energy is constructed, where m represents the number of frequency windows of the wavelet basis function and n denotes the amount of signal data.

$$P_{n\times m}(WT_f, Wf_t) = [(\psi_{A,t})^T]_{n\times 1} A_{n\times m} [\psi_{A,f}]_{1\times m} \quad (2)$$

Where, $[(\psi_{A,t})^T]_{n\times 1}$ denotes the time-domain operator of the time-frequency energy matrix, and the number of rows $n$is equal to the amount of signal data; $[\psi_{A,f}]_{1\times m}$ represents the frequency-domain operator of the time-frequency energy matrix, and the number of columns m is equal to the number of frequency windows of the wavelet basis function; $A_{m\times n}$ is the time-frequency Window function matrix for the energy matrix. Each row vector in the window function matrix corresponds to m wavelet basis functions $[\psi_{A_i,t'_i}(t_i, \Delta\frac{f_m}{m}), \ldots, \psi_{A_i,t'_i}(t_i, \Delta f_m)]$ $(i = 1, 2, \ldots n)$ with the same frequency bandwidth, and f_m represents the maximum sampling frequency of the acquisition system. $\{\Delta\frac{f_m}{m}, \Delta\frac{2f_m}{m}, \ldots, \Delta f_m = [\frac{(m-1)f_m}{m} \sim \frac{(m+1)f_m}{m}]\}$ indicates the corresponding frequency range of each frequency window, and $\frac{f_m}{m}, \frac{2f_m}{m}, \ldots, \frac{(m-1)f_m}{m}, f_m$ is the center frequency of each frequency window. The wavelet time-frequency decomposition process is equivalent to opening the number of $m$windows in the frequency domain, and its frequency resolution is always greater than $\frac{f_m}{m}$.

To detect the underwater diffusion reflection echo signals, the underwater laser time-frequency analysis based on wavelet transform is applied. In this method, a time-frequency energy matrix of the echo signal is constructed by multi-layer wavelet time-frequency decomposition. For pulsed light underwater detection, the area with higher frequency in the time-frequency energy matrix was selected as target echo andused to extract the waveform in time domain by integrating the energy distribution in the matrix with respect to frequency. The corresponding delay of the target is determined by peak detection method, and the target distance information is retrieved.

III. Result

Fig. 3 illustrates the experimental system. The Helios 532-3-50 pulsed laser (US, Coherent) was used as the emission source of the system. Laser output light index: Under the repetition rate of 50 kHz, the average power of the pulsed light became stable at about 3 W, the pulse width was less than 1ns, and the divergence angle was 0.5 mrad. Most of the incident light got reflected by a 45-degree mirror (532 nm >99%) into the 3 m water tank, and a nominal amount of the incident light was transmitted into an APD detector with a low gain bandwidth of 1 GHz as the reference light. The target in the water was a white frosted plastic board. The reflected signal was received by the lens group of the receiving system and further focused on

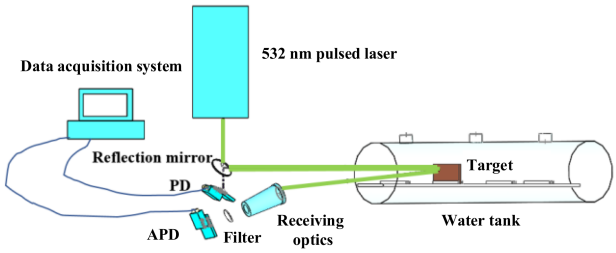

Fig. 3. Laser underwater detection optical system.

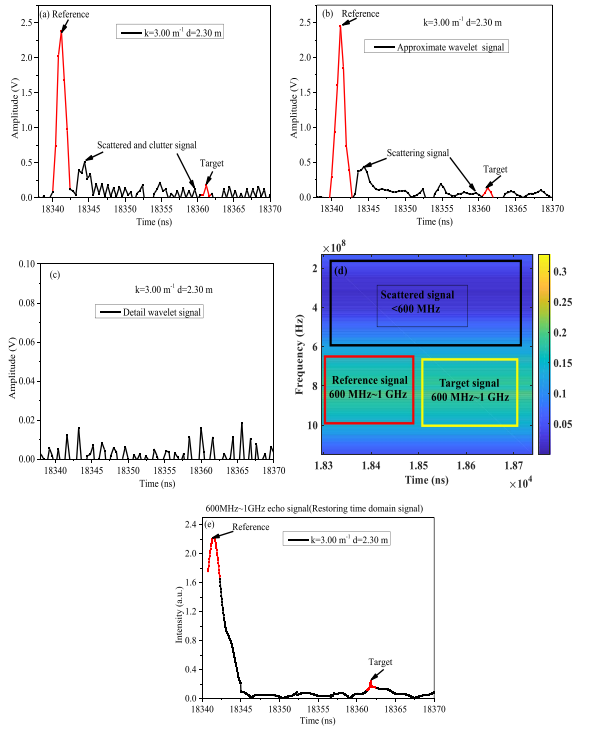

Fig. 4. Reference and target echo signal waveforms and corresponding calculation results (a) are the reference and target echo signal waveforms, (b) and (c) are the approximate echo waveforms and detailed echoes of the first layer of wavelet time domain decomposition, respectively, (d) and (e) are the wavelet time-frequency decomposition results and restoration time domain results of (b), respectively.

the APD detector. The receiver APD detector had a high-gain amplifier of the bandwidth of [50 kHz∼1.5 GHz]. The target echo signal received by the APD detector and the reference signal received by the low-gain PD detector were combined by input to the data acquisition system.

A data acquisition system with a sampling rate of $f_m = 2.5$ GHz and bandwidth of 1 GHz was used to acquire the output time-domain signal. Fig. 4(a) demonstrates a diffusion target echo waveforms, when the water attenuation coefficient was 3.00 m^{-1}, and the target was placed at the 2.30 m from the reference. Fig. 4(b) and (c) depict the first-layer wavelet time-domain decomposition results of the signal in Fig. 4(a). Fig. 4(b) highlights the approximate signal of the first layer wavelet time-domain decomposition, which corresponds to the signal frequency range [0∼1.25 GHz]. The pulse width of the emission source was not more than 1ns, corresponding to the upper-frequency limit

$f_{top} \geq 1$ GHz of the spectrum, and the frequency resolution $f = \frac{f_{top}}{2(f_m/f_{top})} \geq 0.2$ GHz (The upper-frequency limit $f_{top} \geq 1$ GHz of the pulse emission source was close to the median frequency of the acquisition system frequency range [0∼2.5 GHz]) of the target signal could be obtained. The detailed signal of the first layer of wavelet time-domain decomposition, which corresponds to the signal frequency range [1.25 GHz∼2.5 GHz], is shown in Fig. 4(c). It can be observed that there is almost no target echo signal in this part. This indicated that the first layer of wavelet time-domain decomposition primarily filtered out the influence of the high-frequency clutter, such as electromagnetic noise. It could be inferred from the above results that the frequency range corresponding to the target signal was chiefly concentrated in the range of $[(1 - f \times N)\text{GHz} \sim 1\ \text{GHz}]$. Fig. 4(d) illustrates the wavelet frequency-domain decomposition result of the signal in Fig. 4(b); the color distribution in the figure denotes the energy intensity, and the energy distribution from low to high corresponds to the color distribution of blue-violet to orange-yellow, respectively. Thus, this method could distinguish the scattered frequency-domain energy region and the signal's frequency-domain energy region in the time-frequency energy matrix of the echo signal. In this time-frequency energy matrix, the yellow area represents high-energy region, and the corresponding frequency range is $(600\ \text{MHz} \sim 1\ \text{GHz})$. The frequency energy distribution of the time-frequency energy matrix further determined the target signal frequency range $[(1 - 0.2 \times 2)\text{GHz} \sim 1\ \text{GHz}]$. As demonstrated in Fig. 4(e), the frequency range $(600\ \text{MHz} \sim 1\ \text{GHz})$ of the time-frequency energy matrix was extracted, and the frequency domain of the time-frequency energy matrix was accumulated to determine the time-domain signal. At room temperature, the refractive index of seawater was approximately 1.339 [34]. Peak detections are carried out on the recovered time-domain signal, as shown in Fig. 4(e). The time difference between the reference peak and the target echo peak was 20.38 ns, and the target distance was 2.283 m.

Assume that the emitted light power is P_0, the target distance is L, and the water attenuation coefficient is a. If the effective receiving area of the system is A, the total efficiency of each optical element of the lidar is η, and the reflectivity of the object is T, the received target echo optical power reads:

$$P = P_0 e^{-2aL} \frac{\eta t A}{L^2} \tag{3}$$

Therefore, different distances correspond to different echo intensities. In addition, when the turbidity changed, the echo intensity certainly also changed accordingly.

Fig. 5(a) demonstrates a diffusion target echo waveforms, when the water attenuation coefficient was 6.00 m^{-1}, and the target was placed at the 1.30 m from the reference. It could be observed that clutter (scattering) appears as a series of protrusions with different intensities and the target echo. The signal was covered by such clutter, and the time-of-flight method cannot be used for distance detection. Fig. 5(b) illustrates the result of performing wavelet time-frequency decomposition on the signal in Fig. 5(a) by extracting the frequency-domain energy of the effective signal and restoring the time-domain. Comparing

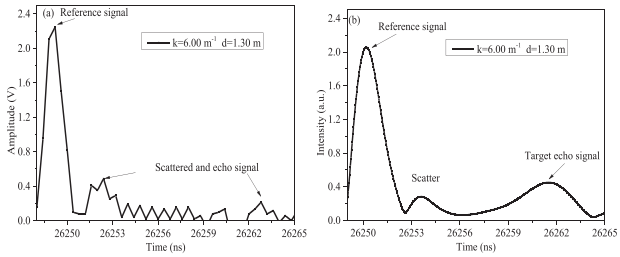

Fig. 5. The effect of the time-frequency analysis ranging method based on wavelet transform on signal processing. 5(a) shows the water attenuation coefficient of 6.00 m^{-1}, the target was placed at 1.30 m for the reference and target diffuse echo signal waveforms. 5(b) is the result of 5(a) extracting the frequency domain energy of the effective signal and restoring the time domain.

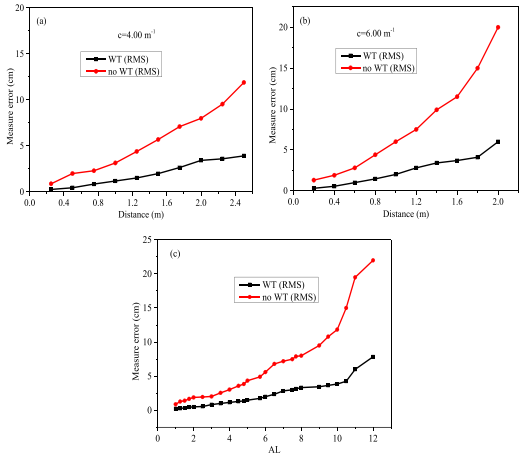

Fig. 6. Comparison of ranging results of underwater diffuse reflection targets by time-frequency analysis ranging method based on wavelet transform and time-of-flight method measurement error and root mean square (a) and (b) are the measurement error, and root mean square of underwater targets at different distances with different attenuation coefficients (c) the measurement error and root mean square of the target in water bodies with varying attenuation lengths.

Fig. 5(a) with (b), the clutter and scattering at a short distance and other positions were weakened, and the target echo signal could be identified. The time-frequency analysis ranging method based on wavelet transform possessed anti-scattering properties. In Fig. 5(b), the peak value detected the echo signal. The corresponding time difference between the reference peak and the target echo peak was 11.52 ns, and the single measurement distance corresponding to the reference and the target was 1.2905 m.

Wavelet transform based on time-frequency analysis and the time-of-flight method could be used for multiple measurement errors and their Root Mean Square (RMS) underwater diffuse reflection targets. The measurement error is the difference between the actual distance of the target and the measured value, as highlighted in Fig. 6(a)∼(c). The emission source was a pulsed laser, the repetition frequency was set to 50 kHz, and average power was 3 W. The pulse width was not more than 1 ns, and the APD detector detected the echo signal. Considering the sensitivity and minimum distinguishable intensity of the data acquisition system, the time-frequency analysis ranging method can be used to detect the distance of more than 10 attenuation lengths. Ideally, the target echo light and the transmitted pulse

light should have the same pulse width, and the echo signal with the time fluctuation corresponding to the measurement error of fewer than 1 ns was regarded as an effective echo signal, and the corresponding measurement error should not be more than 10 cm. The RMS method evaluates the error range between the detected and actual distance. The ranging accuracy within 10 attenuation lengths is better than 4 cm.

IV. Conclusion

This paper proposes a time-frequency analysis method based on wavelet transformation in an underwater light detection and ranging system. The ranging method first performed multi-layer wavelet time-domain decomposition, which filtered out high-frequency electromagnetic noise. Then, a time-frequency energy matrix was constructed by binary spline interpolation based on energy conservation. A high frequency area with strong echo intensity was chosen to restore the time domain waveform of target reflected echo due to target reflection can keep the high frequency component whereas the multiple clutters behave as a low-pass filter. In such a way, the area corresponds to echo from multiple clutters was discarded thus the influence from the scattering clutter was reduced. The ranging error in a puled under water lidar system was reduced from 12 cm to less than 4 cm at an AL of 10. The ranging method can enhance the underwater laser detection and ranging capability.

Acknowledgment

The authors would like to thank the anonymous reviewers for their valuable suggestions.

References

[1] N. Alem, F. Pellen, G. L. Brun, and B. L. Jeune, "Extra-cavity radiofrequency modulator for a lidar radar designed for underwater target detection," *J. Appl. Opt.*, vol. 56, no. 26, pp. 7367–7372, 2017.

[2] A. Matwyschuk, "Impact of a distance estimation error inducing a visualized zone gap on the target illuminance in range-gated active imaging," *J. Appl. Opt.*, vol. 53, no. 1, pp. 44–50, 2014.

[3] D. Comite and N. Pierdicca, V. Kabashnikov, and B. Kuntsevich, "Distance determination based on the delay time-intensity profile analysis in range-gated imaging," *J. Appl. Opt.*, vol. 56, no. 30, pp. 8378–8384, 2017.

[4] A. Matwyschuk, "Combination of the two styles of the multiple-wavelength range-gated active imaging principle for four-dimensional imaging," *J. Appl. Opt.*, vol. 59, no. 25, pp. 7670–7679, 2020.

[5] X. Yin, H. Cheng, K. Yang, and M. Xia, "Bayesian reconstruction method for underwater 3D range-gated imaging enhancement," *J. Appl. Opt.*, vol. 59, no. 2, pp. 370–379, 2020.

[6] M. Wang et al., "Range-intensity-profile prior dehazing method for underwater range-gated imaging," *J. Opt. Exp.*, vol. 29, no. 5, pp. 7630–7640, 2021.

[7] S. P. O'Connor, L. J. Mullen, and B. Cochenour, "Underwater modulated pulse laser imaging system," *J. Opt. Eng.*, vol. 53, no. 5, 2014, Art. no. 051403.

[8] C. Brandon, M. Kaitlyn, M. Keith, J. Eric, D. Kaitlin, and M. Linda, "Propagation of modulated optical beams carrying orbital angular momentum in turbid water," *J. Appl. Opt.*, vol. 55, no. 31, pp. C34–C38, 2016.

[9] W. B. Wang, R. Goza li, L. Shi, L. Lindwasser, and R. R. Alfano, "Deep transmission of Laguerre–Gaussian vortex beams through turbid scattering media," *J. Opt. Lett.*, vol. 41, no. 9, pp. 2069–2072, 2016.

[10] Y. Q. Liao et al., "Numerical simulation of performance improvement of underwater lidar by using a spiral phase plate as spatial filter," *IEEE Photon. J.*, vol. 14, no. 1, Feb. 2022, Art. no. 6800405.

[11] R. Nian, F. Liu, and B. Bo, "A nearly underwater artificial vision model in ocean investigations via independent component analysis," *J. Sensors*, vol. 13, no. 7, pp. 9104–9131, 2013.

[12] D. W. Illig, W. D. Jemison, and L. J. Mullen, "Independent component analysis for enhancement of an FMCW optical ranging technique in turbid waters," *J. Appl. Opt.*, vol. 55, no. 31, pp. C25–C33, 2016.

[13] A. Maccarone et al., "Underwater depth imaging using time-correlated single-photon counting," *J. Opt. Exp.*, vol. 23, no. 26, pp. 33911–33926, 2015.

[14] A. Matwyschuk, "Impact of a distance estimation error inducing a visualized zone gap on the target illuminance in range-gated active imaging," *J. Appl. Opt.*, vol. 53, no. 1, pp. 44–50, 2014.

[15] Y. Ma, S. Li, W. H. Zhang, Z. Y. Zhang, R. Liu, and X. H. Wang, "Theoretical ranging performance model and range walk error correction for photon-counting lidars with multiple detectors," *J. Opt. Exp.*, vol. 26, no. 12, pp. 15924–15934, 2018.

[16] K. J. Hua, B. Liu, L. Fang, H. C. Wang, Z. Chen, and Y. Yu, "Detection efficiency for underwater coaxial photon-counting lidar," *J. Appl. Opt.*, vol. 59, no. 9, pp. 2797–2809, 2020.

[17] K. J. Hua, B. Liu, L. Fang, H. C. Wang, Z. Chen, and J. C. Luo, "Correction of range walk error for underwater photon-counting imaging," *J. Opt. Exp.*, vol. 28, no. 24, pp. 36260–36273, 2020.

[18] Z. M. Li et al., "Thresholded single-photon underwater imaging and detection," *J. Opt. Exp.*, vol. 29, no. 18, pp. 28124–28133, 2021.

[19] Y. Q. Yang et al., "Binning-based local-threshold filtering for enhancement of underwater 3D gated range-intensity correlation imaging," *J. Opt. Exp.*, vol. 29, no. 6, pp. 9385–9395, 2021.

[20] Y. Z. Liu and B. Zhao, "Phase-shift correlation method for accurate phase difference estimation in range finder," *J. Appl. Opt.*, vol. 54, no. 11, pp. 3470–3477, 2015.

[21] S. Li, Z. Y. Zhang, Y. Ma, H. M. Zeng, P. F. Zhao, and W. H. Zhang, "Ranging performance models based on negative-binomial (NB) distribution for photon-counting lidars," *J. Opt. Exp.*, vol. 27, no. 12, pp. A861–A877, 2019.

[22] J. Yang, Y. Ma, S. Li, X. Y. Liu, W. H. Zhang, and Z. Y. Zhang, "Theoretical model considering optimal ranging performance and energy efficiency for photon-counting lidars with multiple detectors," *J. Appl. Opt.*, vol. 60, no. 28, pp. 8838–8850, 2021.

[23] Z. Y. Zhang et al., "Ranging performance model considering the pulse pileup effect for PMT-based photon-counting lidars," *J. Opt. Exp.*, vol. 28, no. 9, pp. 13586–13600, 2020.

[24] A. Matwyschuk, "Multiple-wavelength range-gated active imaging in superimposed style for moving object tracking," *J. Appl. Opt.*, vol. 56, no. 27, pp. 7766–7773, 2017.

[25] Z. X. Peng, B. Z. Zhou, H. Chen, Z. Zhang, and P. Tan, "Satellite-borne laser underwater target detection based on single photon in-depth research," *Laser. Appl. Tech.*, vol. 48, no. 7, pp. 134–142, 2018.

[26] A. Matwyschuk, "Combination of the two styles of the multiple-wavelength range-gated active imaging principle for four-dimensional imaging," *J. Appl. Opt.*, vol. 59, no. 25, pp. 7670–7679, 2020.

[27] Y. Chen, W. G. Shen, and Z. M. Li, "Underwater transmission of high-dimensional twisted photons over 55 meters," *PhotoniX*, vol. 1, no. 1, pp. 1–11, 2020.

[28] V. D. Vrabie, J. I. Mars, and J. L. Lacoume, "Modified singular valued ecomposition by means of independent component analysis," *J. Signal Process.*, vol. 84, no. 3, pp. 645–652, 2004.

[29] L. T. Bang, Z. Ali, P. D. Quang, J. H. Park, and N. Kim, "Compression of digital hologram for three-dimensional object using wavelet-bandelets transform," *J. Opt. Exp.*, vol. 19, no. 9, pp. 8019–8031, 2011.

[30] S. J. Wang, Z. Gao, G. Y. Li, and Z. Feng, "Adaptive pulse oximeter with dual-wavelength based on wavelet transforms," *J. Opt. Exp.*, vol. 21, no. 20, pp. 23058–23067, 2013.

[31] Y. C. Kim, K. H. Jin, J. C. Ye, J. W. Ahn, and D. Su. Yee, "Wavelet power spectrum estimation for high-resolution terahertz time-domain spectroscopy," *J. Opt. Soc. Korea*, vol. 15, no. 1, pp. 103–108, 2011.

[32] S. Ghosh et al., "Differing self-similarity in light scattering spectra: A potential tool for pre-cancer detection," *J. Opt. Exp.*, vol. 19, no. 20, pp. 19717–19730, 2011.

[33] X. H. Zou et al., "Accuracy improvement of quantitative analysis in laser-induced breakdown spectroscopy using modified wavelet transform," *J. Opt. Exp.*, vol. 22, no. 9, pp. 10233–10238, 2014.

[34] W. Jun, S. M. Huang, Z. Hang, W. X. Ping, and X. U. Meng, "Simultaneous measurement of chlorella solution concentration and absorption coefficient," *Acta Photonica Sinica*, vol. 45, no. 2, 2016, Art. no. 0212001–5.